Make tenses consistent - often alternating between present and past tenses

Consistency test of precipitating ice cloud retrieval properties obtained from the observations of different instruments operating at Dome-C (Antarctica)

Gianluca Di Natale[1], David D. Turner[2], Giovanni Bianchini[1], Massimo Del Guasta[1], Luca Palchetti[1], Alessandro Bracci[3,4], Luca Baldini[3], Tiziano Maestri[4], William Cossich[4], Michele Martinazzo[4], and Luca Facheris[5]

[1]National Institute of Optics, CNR-INO, Via Madonna del Piano 10, Sesto Fiorentino, Firenze, Italy
[2]NOAA/OAR/Global Systems Laboratory, Boulder, Colorado, USA
[3]Institute of Atmospheric Sciences and Climate, CNR-ISAC, Rome, Italy
[4]Department of Physics and Astronomy "Augusto Righi", Alma Mater Studiorum University of Bologna, Bologna, Italy
[5]Department of Information Engineering, University of Florence, Via di Santa Marta 3, Firenze, Italy

Correspondence: Gianluca Di Natale (gianluca.dinatale@ino.cnr.it)

Abstract.

Selected case studies of precipitating ice clouds at Dome-C (Antarctic Plateau) are used to test a new approach for the estimation of ice cloud reflectivity at 24 GHz (12.37 mm ~~of~~ wavelength) using ground-based far infrared spectral measurements from the REFIR-PAD Fourier transform spectroradiometer and backscattering/depolarization lidar profiles. The resulting reflectivity is evaluated with the direct reflectivity measurements provided by a co-located micro rain radar (MRR) operating at 24 GHz, ~~which~~ that is able to detect falling crystals with large particle size, typically above 500 μm .

To obtain the 24 GHz reflectivity, we used the particle effective diameter and the cloud optical depth retrieved from the far infrared spectral radiances provided by REFIR-PAD and the tropospheric co-located backscattering lidar to calculate the modal radius and the intercept of the particle size distribution. From these, the theoretical reflectivity at 24 GHz is obtained by integrating the size distribution over different microwave cross sections for various habit crystals provided by Eriksson et al. (2018) databases. From the comparison with the radar reflectivity measurements, we found that the column-like habits and the plates/columnar crystal aggregates show the best agreement with the MRR observations. The presence of (hexagonal) pristine hexagonal columns is confirmed both by the presence of 22° solar halos, detected by the HALO-CAMERA~~,~~ and ~~by~~ both the crystal images taken by the ICE-CAMERA~~,~~ that are operating in proximity of REFIR-PAD and the MRR. The average crystal lengths obtained from the retrieved size distribution are also compared to ~~the ones~~ those estimated from the ICE-CAMERA images. The agreement between the two results confirms that the retrieved parameters of the particle size distributions correctly reproduce the observations.

1 Introduction

The importance of clouds in the global climate is shown by many studies and is strongly related to their role in modulating the incoming solar radiation in the shortwave (0.2-5 μm) and the outgoing emission from the Earth in the longwave (5-100 μm) broadband

broadband Need to define what is meant by cloud effect

bands. The cloud effect can be either a net cooling if they are enough thick to reflect most of the incoming radiation back to space or a net warming if they absorb more radiation than they reflect; therefore they acting as regulators of the Earth Radiation Budget (ERB) (Kiehl and Trenberth, 1997; Solomon, 2007). The effect of clouds on the ERB is still not completely assessed; for example, recent studies demonstrated that small ice crystals and optical depth greater than 10 or large particles and optical depths less than 10 can yield to a net cooling as low as -40 W m^{-2} or a net warming as high as +20 W m^{-2} (Baran, 2009). Therefore, more accurate statistics of the cloud optical and microphysical properties are needed to better characterize their radiative effect; this is especially true for ice clouds, which represent the greatest challenge because of the extremely inhomogeneous composition of crystal sizes and habits. Ice cloud properties in the polar regions are the least well known and improved characterizations of these properties are much needed.

A realistic parameterization of the Antarctic ice clouds has proven to improve the performance of the Global Circulation Models (GCMs) (Lubin et al., 1998). The radiative forcing caused by these clouds influences the Surface Radiation Budget (SRB) and thereby the surface temperature (Stone et al., 1990), which is a relevant aspect of the Antarctic environment.

been shown

an important component

Mixed phase clouds greatly impact the SRB (Lawson and Gettelman, 2014; Korolev et al., 2017), since the atmospheric radiation balance is very sensitive to the distribution of cloud phase as pointed out in Shupe et al. (2008). These clouds represent a three-phase system consisting of water vapour, ice crystals, and supercooled water droplets at temperatures between 0°C and -40°C in which the glaciation process is the result of the ice growth at the expense of the liquid droplets, also known as the Wegener–Bergeron–Findeisen (WBF) mechanism (Korolev and Isaac, 2003). Mixed-phase clouds are very common in polar regions (Turner et al., 2003; Cossich et al., 2021) but they also occur at lower latitudes as discussed in Costa et al. (2017).

The uncertainties in the cloud radiative properties represent the main contributor to the biases in the radiative fluxes both at the top of the atmosphere and at the surface (Rossow et al., 1995). These uncertainties are mostly due to the lack of spectrally resolved measurements in the Far InfraRed (FIR) both from ground-based sites and from airborne instruments, as well as to the scarceness of in-situ measurements of size and habit distributions of the ice crystals.

Suggest updating references, perhaps from the CERES team, Norman Loeb and others

Problematic

The representation of the radiative properties of cirrus clouds is tricky because of the presence of myriad of different crystal habits and sizes (Baran, 2009). This inhomogeneity is strongly related to the supersaturation condition (Korolev et al., 2017), which depends on the atmospheric temperature, humidity, and vertical wind (Keller and Hallett, 1982). These clouds are also sensitive to the aerosol concentration and composition, which act as ice nucleation particles and cloud condensation nuclei (Fan et al., 2017). The complexity of the habit crystals is well described in detail in Bailey and Hallett (2009), where the single crystals and polycrystalline regimes (columnar and plate-like) are shown as a function of the ice supersaturation and temperature.

that

It is clear that the FIR portion of the spectrum plays an important role in the longwave radiative budget since even in clear sky conditions more than 50% of the entire flux comes from this spectral region; the contribution can exceed 60% at poles because of the extremely dry conditions and the low temperatures. Furthermore, FIR spectrum is strongly modulated by the clouds and, in particular, shows an important feedback from cirrus clouds (Harries et al., 2008) since this region is very sensitive to the microphysics (Yang et al., 2003a; Baran, 2007).

in polar regions

the

Elaborate on what is meant by the sensitivity to microphysics (also should include optical properties)

Different studies pointed out that the total downwelling radiative flux in the internal regions of Antarctica, including Dome-C, varies from 50 to 220 W m^{-2} (Bromwich et al., 2013; Di Natale et al., 2020) because of the cloud forcing. In particular,

Should include a brief discussion of cloud forcing, perhaps in the earlier discussion of cloud radiative effects

the FIR component (below 667 cm^{-1}) reaches the 75% of the total flux for thinner clouds and reduces to 55% for the thicker ones, since the longwave radiative fluxes (LRF) strongly depend on the Ice/Liquid Water Content (IWC/LWC) ~~inside~~ the cloud (Di Natale et al., 2020).

The study of the downwelling FIR spectrum by means of ground-based, zenith-looking observations is extremely important ~~in order~~ to assess the emission component of the ERB providing the complementary component of the spectral radiance at the top of the atmosphere (TOA). These kind of measurements need to be performed from extremely dry sites, such as high mountains or polar regions, due to the opacity of the atmosphere (Turner and Mlawer, 2010) so there are difficult constraints on where these observations can be made. On the other hand, ~~they allow to~~ detect the signal coming from the upper part the atmosphere~~,~~ where clouds occur, with a greater contrast with respect to the nadir-looking observations, since the background signal comes from ~~the~~ cold space and not from the emitting surface.

During last two decades, measurements of the downwelling longwave radiation, including in the FIR, have been used to study the cirrus cloud radiative properties both at mid-latitudes (Palchetti et al., 2016; Di Natale et al., 2021; Maestri et al., 2014) and in polar regions, in particular in Arctic (Garrett and Zhao, 2013; Intrieri et al., 2002; Ritter et al., 2005) and Antarctica (Maesh et al., 2001a, b; Palchetti et al., 2015; Di Natale et al., 2017; Rowe et al., 2019; Rathke et al., 2002; Maestri et al., 2019).

Since December 2008, several instruments have been installed at Dome-C and operated continuously ~~in order~~ to characterize the microphysical properties of ice clouds over Antarctica. Starting in 2018, the FIRCLOUDS (Far InfraRed closure experiment for Antarctic CLOUDS) project, funded by the Italian National Program for the Antarctic Research (PNRA), has been providing statistics of the radiative properties of the Antarctic clouds ~~in order~~ to evaluate the current parameterizations of ice and mixed phase clouds through the intercomparison of the retrieval products obtained from different kind of measurements.

This paper describes a new approach to compare the clouds radiative and physical properties retrieved from spectral FIR measurements against microwave radar observations using data from 14 days of selected observations of precipitating ice clouds observed between 2019-2020 at Dome-C. Section 2 presents and describes the instruments operating at Dome-C, and section 3 discusses the methodology used to compare the 24 GHz radar reflectivity observations with those retrieved from the FIR radiance spectra. The results are discussed in section 4, with a detailed comparison from four selected days ~~.~~ Finally, in section 5 the conclusions are drawn.

2 Instruments and observations

2.1 REFIR-PAD Fourier spectroradiometer and tropospheric backscattering/depolarization lidar

The Radiation in Far InfraRed - Prototype for Applications and Development (REFIR-PAD) (Bianchini et al., 2019) is a Fourier transform spectroradiometer (FTS) ~~which~~ that detects the spectral radiance emitted by the atmosphere in the broad band between 100-1500 cm^{-1} (6-100 μm) with a spectral resolution of 0.4 cm^{-1} . REFIR-PAD was installed inside the PHYSICS shelter at Concordia base at Dome-C, where it views the atmosphere through a 1.5 m chimney. It was installed in December 2011, and has operated continuously in unattended mode since, providing spectral radiances every $\sim$12 minutes. The radiance calibration is performed for each scene measurement through two black bodies stabilized in temperature, one hot and one cold, forming

the calibration unit, while the thermal background is stabilized by means of a reference black body at room temperature. The interferometer is in Mach-Zehender configuration with two inputs and two outputs, which enables the best performance. The total field of view (FOV) is equal to 115 mrad, with a internal beam divergence of about 0.00087 sr and a throughput of about 0.0035 cm^2 sr. The complete instrument specifications and description are thoroughly described in Bianchini et al. (2006, 2019) and Palchetti et al. (2015).

Figure 1. Left side: REFIR-PAD Fourier transform spectroradiometer inside the PHYSICS shelter with the 1.5 m chimney connecting the instrument with outside. Right side: output windows of the tropospheric lidar on the roof of the shelter.

The backscattering/depolarization tropospheric lidar is collocated inside the PHYSICS shelter. It was installed in 2008, and has operated in unattended mode providing the backscattering and depolarization signal profiles with a temporal frequency of 10 minutes. The instrument uses the spectral channel at 532 nm of wavelength to provide the backscattering signal and the depolarization. Fig. 1 shows the REFIR-PAD Fourier transform spectroradiometer inside the PHYSICS shelter and the aperture of tropospheric lidar on the roof.

the

2.2 Micro Rain Radar (MRR)

The Micro Rain Radar-2 (MRR, Metek GmbH, Germany), a profiling Doppler radar, has been operating at Concordia station at Dome-C since December 2018. It was installed on the roof of the PHYSICS shelter in a zenith-looking observation geometry. It operates at 24 GHz, measuring Doppler power spectra in 64 bins over 32 vertical range bins that~~, for Concordia installation,~~ were set to a width of 40 meters. MRR has a compact design being composed of a dish with a diameter of ∼60 cm and a small enclosure containing both a transmitting and receiving ~~transmitting a receiving~~ apparatus. It is characterized by low power consumption and high robustness, making it suitable for deployment in remote regions for long-term unattended measurements. In fact, the MRR is a quite popular instrument for precipitation measurements in Antarctica, in spite of the relatively low sensitivity (Bracci et al., 2022). The

post-processing MRR procedure by Maahn and Kollias (2012) that partially improves the sensitivity of the system and removes spectra aliasing has been adopted.

An automatic data transfer system provides daily measurements directly to the storage server at the National Institute of Optics (CNR-INO) in Florence.

Figure 2. Left side: PHYSICS shelter at Concordia station. Right side: Micro Rain Radar (MRR) installed in 2018 on the roof of the shelter.

Fig. 2 shows on the left side the PHYSICS shelter at Concordia station, where REFIR-PAD spectroradiometer and the tropospheric lidar are installed; on the right side the MRR, which is installed on the roof.

2.3 ICE- and HALO-CAMERA

The ICE-CAMERA (Del Guasta, 2022) is an optical imager mounted on the roof of the PHYSICS shelter. It is able to routinely image falling ice crystals by freezing them on a screen, rapidly photographing them, and then sublimating the deposited particles by heating the screen in a regular cycle. The photographs are analyzed to sort and classify the precipitating ice crystals depending on their habit and sizes. A MATLAB software routine performs the automatic processing of the images: it subtracts the background, enlarges and reduces the binary image, deletes the edge objects, eliminates the single grains, creates and enlarges the grains bounding boxes, and finally sorts the grains depending on the increasing size for graphic use. In the last step, the software calculates the contour and the skeletonization of the remaining grains.

HALO-CAMERA is a sky imager installed on the shelter roof used for monitoring the solar and lunar halos generated by the floating ice crystals. These halos occur because the scattering phase function at visible wavelength of particular ice crystals habits has two peaks at 22° and 46° scattering angles. Fig. 3 shows the two imagers deployed on the roof of the PHYSICS shelter at Concordia station.

wavelengths of pristine hexagonal ice

In the work by Lawson et al. (2006), the images of ice crystals were recorded at the South Pole (Antarctica) by using two ground-based cloud particle imagers (CPIs) jointly with the LaMP (French Laboratoire de Meteorologie Physique) polar nephelometer, which measured the ice crystal phase function. In that work, it was found that the phase function shows the peak at 22° when column-like and plate-like habits occur, while is smoother in case of rosette-like shape. We know that the presence of the peaks in the phase scattering function at visible wavelengths does not depend on the particular crystal habit but on the

Figure 3. Left side: ICE-CAMERA mounted on the roof of the PHYSICS shelter. Right side: HALO-CAMERA installed on the handrail at the edge of the shelter.

roughness of the crystal surface (Yang et al., 2013); the fact that Lawson et al. (2006) did not measure halos in the presence of bullet rosettes is probably related to a rougher crystal surface occurring during the formation of these particular crystals. In summary, we will use the evidence of halo formation as a good indicator of the occurrence of column-like crystals in the Antarctic environment.

Suggest "hexagonal crystals" because it could also be plate-like particles

3 Methodology

The REFIR-PAD retrieved cloud products are used to derive an estimation for the equivalent reflectivity Ze, which can be compared with those obtained from MRR spectra. We used the cloud parameters, such as the ice optical depth (OD_i) at visible wavelengths and the ice effective diameter (D_{ei}), to derive the intercept (N_o) and the modal radius L_m of the particle size distribution (PSD). The PSD ($n(L)$) was assumed as Γ-like distribution with exponent μ and the width associated to L_m defined as $\sigma = 1/(3+\mu) = 0.1$, assuming $\mu = 7$ (Platnick et al., 2017; Matrosov et al., 1994; Turner, 2005). ~~Thus, the expression of the size distribution results~~:

The size distribution is expressed as:

$$n(L) = N_o L^{\mu} e^{-(3+\mu)\frac{L}{L_m}} \tag{1}$$

and the mode of the distribution is given by $(\frac{\mu}{3+\mu})L_m$. Then, we define the effective diameter following Yang et al. (2005):

$$D_{\text{ei}} = \frac{3}{2}\frac{\int_{L_{\text{min}}}^{L_{\text{max}}} V(L)n(L)dL}{\int_{L_{\text{min}}}^{L_{\text{max}}} A(L)n(L)dL} \tag{2}$$

where V and A denote the particle volume and projected area, respectively. And L is the length of assumed crystal in the given size bin

Once the PSD is defined, the effective MRR reflectivity is obtained by integrating the backscattering cross sections at 24 GHz (12.37 mm) tabulated in the database provided by Eriksson et al. (2018) over the PSD for different assumed crystal habits.

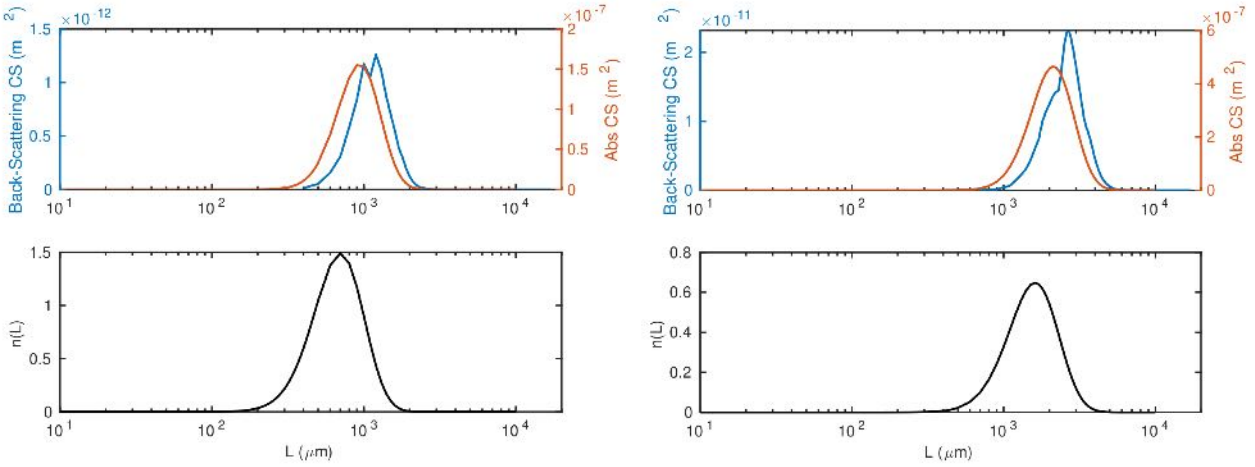

Figure 4. Left side: normalized PSD with L_m = 1000 μm (lower panel) and the relative backscattering cross section at 24 GHz and absorption cross sections at 400 cm^{-1} as a function of particle dimensions (upper panel). Right side: same as left side but for a PSD defined by L_m = 2300 μm .

Figure 4 shows the backscattering and absorption cross sections contribution as a function of the particle dimension (L), for two different normalized particle size distribution with L_m = 1000 μm and L_m = 2300 μm respectively, corresponding to effective diameters D_e equal to 100 and 300 μm , as ~~we can see from~~ shown in Fig. 5.

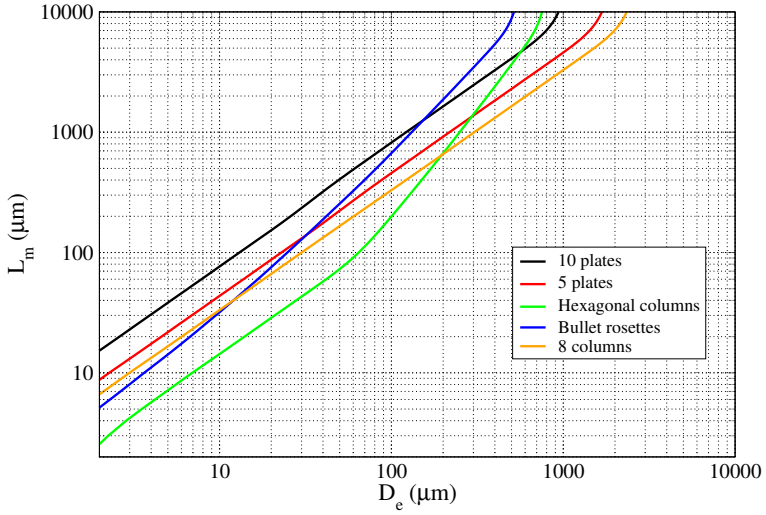

Figure 5. Relationship between the effective diameter (D_{ei}) and the modal radius (L_m) of the particle size distribution for the various ice crystal habits. Note: these are actually very large differences because these are log-log plots. This demonstrates the importance of the habit on the microphysical properties of the ice cloud.

The results are obtained using the single particle optical properties of the large plate aggregates at 24 GHz for the backscattering and at 400 cm^{-1} for the absorption cross sections. The figure shows that the largest crystals of the assumed PSDs (lower panels) provide the biggest contribution to the total backscattering cross section (representative of the MRR measurement). A similar result is obtained for the absorption cross section at 400 cm^{-1} (assumed as the key parameter of the REFIR-PAD measurements at FIR), which, however, presents a peak slightly shifted towards the smaller dimensions. A considerable overlap between the two curves suggests that it is possible to obtain information on a large part of the PSD from FIR spectral measurements.

Which figure?

The MRR signal represents an indicator of the presence of large ice particles, while the infrared downwelling spectral radiance (R_ν) measured by REFIR-PAD shows more sensitivity to changes in smaller particles. On the left side of Fig. 6 we can see that the absolute values of the downwelling spectral radiance derivatives calculated with respect to D_{ei} for values of OD_i equal to 0.5 and 2 (upper and lower panels) at 400 cm^{-1} (panels a and c) of wavenumber ν are more intense than at 830 cm^{-1} (panels b and d), as much as one order of magnitude. The simulations are generated by placing an ice cloud close to the ground and the top at 5 km a.s.l., which is representative of the precipitating ice clouds we observed. From panels a and c of Fig. 6 we can also notice that for D_{ei} larger than 100 μm the derivatives calculated for the 10 plates aggregate habit shows the highest sensitivity. The color map on the right side shows that there is a good sensitivity in the FIR region (400 cm^{-1}) for D_{ei} as high as about 300 μm for optical depth lower than 6. All this suggests us that 10 plates aggregate could be the more suitable habit for retrieving atmospheric scenarios with large ice particles up to 300 μm for OD_i lower than 6.

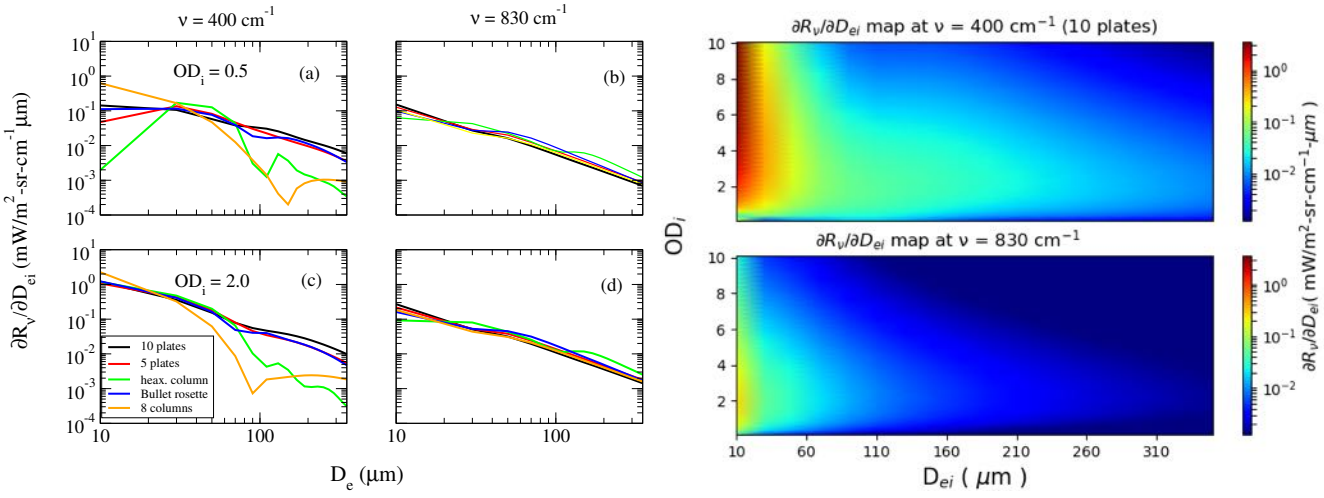

Figure 6. Left side: absolute values of the downwelling spectral radiance derivatives with respect to the effective diameter simulated for two precipitating ice clouds with optical depth 0.5 (upper panels) and 2 (lower panels), at wavenumbers (ν) 400 cm^{-1} (panels a and c) and 830 cm^{-1} (panels b and d) for five different crystal habits. Right side: same derivatives of the left side but only for 10 plates aggregate and for multiple optical depth values ranging between 0.1 and 10.

For my old eyes, it is a bit difficult to make out the detail in the 4-panels on the left - would it be possible to separate the left figure from the right figure so that it appears larger in the text?

This is quite interesting because actual observations from the Antarctic may not be widely known. It would be useful to include a summary of the types of ice particles found in the ICE-CAMERA photographs in different conditions.

In this work, we assumed that plate-like and droxtal-like crystals were not present, since at temperatures below -20°C, the prevalent regime is columnar because the ice supersaturation and the crystal growth rate are generally higher as pointed out in Bailey and Hallett (2009). Moreover, at these temperatures, plates and droxtals show a low growth rate (Bailey and Hallett, 2009) and then have smaller sizes, below 60 and 100 μm , respectively (Yang et al., 2013; Lawson et al., 2006). Also, their occurrence is mostly found during diamond dust events and they were rarely observed in the ICE-CAMERA photographs during the precipitation events detected with the MRR. In the next section, we will show the low dependence on the habit type of the particle size distribution when the maximum crystal length stays in the range between 600 μm and 1800 μm . This peculiarity, and the fact that for the 10 plate aggregates the downwelling spectral radiance is much more sensitive to the D_{ei} at the largest values above 100 μm with respect to the other habits, will be exploited to retrieve the effective diameter of the larger particles as discussed in the next section.

The average absorption/extinction efficiencies ($\langle Q_{\mathrm{a,ei}} \rangle_\nu$), the single scattering albedo ($\langle \omega_{\mathrm{i}} \rangle_\nu$), and the asymmetry factor ($\langle g_{\mathrm{i}} \rangle_\nu$) at the wavenumber ν used to simulate the spectral radiances in the presence of ice clouds were calculated by assuming the PSD ($n(L)$) in Eq. (1). Thus, the $\langle Q_{\mathrm{a,ei}} \rangle_\nu$ are given by (Yang et al., 2005):

$$\langle Q_{\mathrm{a,ei}} \rangle_\nu = \frac{\int_{L_{min}}^{L_{max}} Q_{\mathrm{a,ei},\nu}(L) A(L) n(L) dL}{\int_{L_{min}}^{L_{max}} A(L) n(L) dL} \tag{3}$$

$$\langle g_{\mathrm{i}} \rangle_\nu = \frac{\int_{L_{min}}^{L_{max}} g_{\mathrm{i}}(L) Q_{\mathrm{si},\nu}(L) A(L) n(L) dL}{\int_{L_{min}}^{L_{max}} Q_{\mathrm{si},\nu}(L) A(L) n(L) dL} \tag{4}$$

$$\langle \omega_{\mathrm{i}} \rangle_\nu = 1 - \frac{\langle Q_{\mathrm{ai}} \rangle_\nu}{\langle Q_{\mathrm{ei}} \rangle_\nu} \tag{5}$$

where $Q_{\mathrm{si},\nu} = Q_{\mathrm{ei},\nu} - Q_{\mathrm{ai},\nu}$ is the scattering efficiency, L_{min} and L_{max} denote the maximum length database limits equal to 2 and 10000 μm , respectively, and $A(L)$ is the projected area of the crystal.

3.1 Retrieval of the particle size distributions from REFIR-PAD spectral radiances

To simulate the downwelling spectral radiance of the atmosphere in the presence of ice clouds, the optical depth of the ice at the infrared wavenumbers is obtained through the relationship (Yang et al., 2003a):

$$\mathrm{OD}_{i,\nu} = \frac{3 \cdot \mathrm{IWP}}{D_{\mathrm{ei}} \rho_i} \frac{\langle Q_{\mathrm{ei}} \rangle_\nu}{2} = \mathrm{OD}_i \frac{\langle Q_{\mathrm{ei}} \rangle_\nu}{2} \tag{6}$$

where $\rho_i = 917$ Kg m^{-3} is the ice density and $\langle Q_{\mathrm{ei}} \rangle_\nu$ the average extinction efficiency at the wavenumber ν. The optical coefficients as a function of L are taken from the database provided by Yang et al. (2013). From Eq. (6), by setting $\langle Q_{\mathrm{ei}} \rangle = 2$ since this factor can be assumed constant because of the large size parameters ($\frac{\pi D_e}{\lambda}$), usually greater than 20 at the typical visible wavelengths, the OD_i is obtained as follows:

$$\mathrm{OD}_i = \frac{3\mathrm{IWP}}{\rho_i D_{ei}} \tag{7}$$

Now we show that within the particle size range of MRR sensitivity, the PSD has in general a very low variability with respect to the crystal habit assumed. The modal radius L_m of the PSD in Eq. (1) can be directly derived from the D_{ei} as shown on the left side of Fig. 5, while the intercept N_o can be obtained by using the expression of the ice water path (IWP):

$$\mathrm{IWP} = \Delta z \cdot \mathrm{IWC} = \Delta z \cdot \rho_i \int_{L_{min}}^{L_{max}} V(L) n(L) dL \tag{8}$$

with $\Delta z = z_t - z_b$ the cloud thickness, the IWC is the average Ice Water Content, and z_t and z_t denote the cloud top and bottom heights (CTH, CBH), respectively, ~~which can be~~ estimated from the lidar signal by applying the polar threshold (PT) algorithm (Van Tricht et al., 2013). Thus, ~~by~~ replacing Eq. (1) in (8) and using Eq. (7) yields ~~to~~:

$$N_o(L_m) = \frac{\mathrm{OD}_i \cdot D_{ei}}{3\Delta z \cdot C(L_m)} \tag{9}$$

expressed in [$\mathrm{m}^{-3}\mathrm{mm}^{-8}$] and the volume factor $C(L_m)$ is given by:

$$C(L_m) = \int_{L_{min}}^{L_{max}} V(L) L^7 e^{-10\frac{L}{L_m}} dL \tag{10}$$

with $V(L)$ volume of the crystals as ~~used in Eq. (2)~~. This result is obtained by assuming the optical depth and the effective diameter constant in the cloud in Eq. (9) and equal to average values.

Fig. 7 shows the curves of the ratio between the intercept (N_o) calculated from Eq. (9) for 10 plates aggregates with respect to those of the other habits of Fig. 6 and 5 as a function of L_m. ~~We can see~~ that in the range of L_m between 500 and 2000 μm where the sensitivity of REFIR-PAD and MRR overlaps, the ratios are close to 1 showing a similar behaviour.

The retrieval of the cloud properties was performed by using the Simultaneous Atmospheric and Cloud Retrieval (SACR) (Di Natale et al., 2020), which is a composed of a forward model (FM) and a retrieval code based on ~~the~~ optimal estimation (OE) approach. The downwelling spectral radiance is simulated in the spectral band between 200–980 cm^{-1} (10–50 μm) through the FM as a function of the atmospheric profiles and the cloud parameters, such as the optical depth and the effective diameter. By using the entire band we can retrieve ~~all~~ the atmospheric variables, since the infrared spectrum shows strong sensitivity to water vapour in the spectral region between 230–600 cm^{-1} (16–43 μm), to the temperature in the band centered at 667 cm^{-1} (15 μm), to the cloud optical depth in the atmospheric window, between 820–980 cm^{-1} (10–12 μm), and to the particle size below 600 cm^{-1} (above 16 μm).

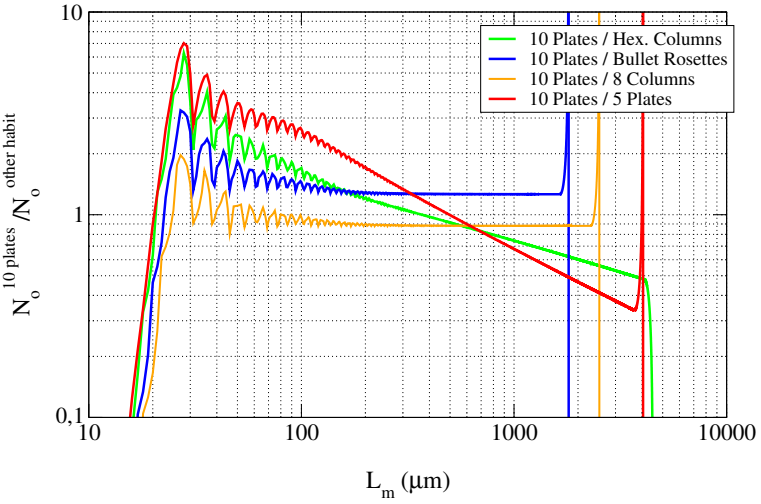

Figure 7. Curves of the ratio between the intercept (N_o) calculated from Eq. (9) for 10 plates aggregates with respect to those of the other habits of Fig. 6 and 5 as a function of L_m .

When liquid supercooled water exists overhead, the retrieval algorithm switches to the mixed-phase clouds retrieval (Di Natale et al., 2021; Turner et al., 2003), where the ice fraction (γ) is also retrieved together with the effective diameter of the water droplets (D_{ew}) in suspension. The ice fraction is defined as (Yang et al., 2003b):

$$\gamma = \frac{\text{IWP}}{\text{IWP+LWP}} \tag{11}$$

where LWP is the Liquid Water Path and, in case of only-ice phase, LWP = 0 and γ is set to 1. In the presence of liquid content D_{ew} is calculated as follows:

$$D_{\text{ew}} = 2\frac{\int_{R_{\text{min}}}^{R_{\text{max}}} R^3 n(R) dR}{\int_{R_{\text{min}}}^{R_{\text{max}}} R^2 n(R) dR} \tag{12}$$

where R is the radius of the droplets and the size distribution $n(R)$ is still a Γ-function like for the ice. The ~~water~~ liquid water optical depth (OD_w) is derived from Eq. (7) by using the parameters for water (LWP, D_{ew}) and the density ρ_w = 1000 kg m^{-3}.

Since the profiles of water vapour and temperature are retrieved simultaneously with the cloud parameters, the final state vector used in the retrieval is given by (Di Natale et al., 2021):

$$\mathbf{x} = (D_{\text{ei}}, \text{OD}_i, \mathbf{U}, \mathbf{T}, \Omega, \beta) \tag{13}$$

for the only-ice case and, by defining the total optical depth OD = OD_i+OD_w, becomes:

$$\mathbf{x} = (D_{\mathrm{ei}}, D_{\mathrm{ew}}, \mathrm{OD}, \gamma, \mathbf{U}, \mathbf{T}, \Omega, \beta) \tag{14}$$

for the case of a mixed phase cloud

~~in case of mixed phase~~, where $\mathbf{U}$ and $\mathbf{T}$ represent the vectors which contain the profile fitted levels of water vapour and temperature (7 for water vapour and 4 for temperature) at fixed pressure levels; Ω is the internal solid angle of the beam divergence which determines the formulation of the Instrument Line Shape (ILS) and it is also fitted ~~in order~~ to take into account the effect of self-apodization; finally, β is a scale factor on the frequency grid introduced to compensate for possible drift of the REFIR-PAD laser reference and for the shift due to the internal finite aperture (Bianchini et al., 2019; Di Natale et al., 2021).

SACR uses a Levenberg-Marquardt iterative algorithm to minimize the cost function (Rodgers, 2000):

$$\chi^2 = (\mathbf{y} - \mathbf{FM}(\mathbf{x}))^T \mathbf{S}_{\mathrm{y}}^{-1} (\mathbf{y} - \mathbf{FM}(\mathbf{x})) + (\mathbf{x} - \mathbf{x}_{\mathrm{a}})^T \mathbf{S}_{\mathrm{a}}^{-1} (\mathbf{x} - \mathbf{x}_{\mathrm{a}}) \tag{15}$$

with $\mathbf{y}$ and $\mathbf{x}_{\mathrm{a}}$ being vectors of the measurements and a priori parameters, respectively. $\mathbf{S}_{\mathrm{y}}$ denotes the Variance-Covariance Matrices (VCM) of the measurements and contains the REFIR-PAD spectral noise, which is given by the square sum of the Noise Equivalent to Signal Ratio (NESR) and the calibration error (Bianchini et al., 2019). The NESR is calculated from the standard deviation of the four uncalibrated spectra provided during each REFIR-PAD measurement; the calibration error is due to the uncertainty on the temperature of the three black bodies (hot, cold, and reference) used for the radiance calibration procedure. The $\mathbf{S}_{\mathrm{a}}$ matrix represents the VCM of the a priori errors associated to the a priori state vector $\mathbf{x}_{\mathrm{a}}$.

The a priori cloud parameters were set to large values equal to 100 μm for the effective diameters and 3 for the optical depth, with a priori error equal to 100%, in order to avoid constraining the retrieval algorithm. We calculated the a priori thermodynamic profiles by interpolating those provided by the daily radiosondes launched at Concordia station. We assumed an a priori error equal to 50% for water vapor profiles and 1% for temperature profiles with a correlation length equal to 2 km to regularize above 9 m of height (Di Natale et al., 2020) and below 5 km. For heights above 5 km where sensitivity both to water vapour and temperature is very low and the information comes mainly from the a priori, a more stringent correlation length equal to 5 km is used to regularize the solution. Note that below 9 m, the levels of the a priori profiles are considered completely uncorrelated and the radiative contribution is mostly given by the temperature and humidity internal to the instrument.

The cost function in Eq. (15) is minimized through the OE and the Levenberg-Marquardt iterative formula given by:

$$\mathbf{x}_{i+1} = \mathbf{x}_i + [\mathbf{K}_i^T \mathbf{S}_{\mathrm{y}}^{-1} \mathbf{K}_i + \gamma_i \mathbf{D}_i + \mathbf{S}_{\mathrm{a}}^{-1}]^{-1} [\mathbf{K}_i^T \mathbf{S}_{\mathrm{y}}^{-1} (\mathbf{y} - \mathbf{FM}(\mathbf{x}_i)) - \mathbf{S}_{\mathrm{a}}^{-1} (\mathbf{x}_i - \mathbf{x}_{\mathrm{a}})] \tag{16}$$

where γ_i is the damping factor at the iteration i, $\mathbf{K}_i$ denotes the Jacobian matrix of $\mathbf{FM}$ and $\mathbf{D}_i$ is a diagonal matrix as described in Di Natale et al. (2020). The convergence is reached when variations on χ^2 are less than 1 ‰. The error of the retrieved parameters is obtained with the relationship:

$$\mathbf{S}_{\mathrm{x}} = (\mathbf{K}^T \mathbf{S}_{\mathrm{y}}^{-1} \mathbf{K} + \mathbf{S}_{\mathrm{a}}^{-1})^{-1} \tag{17}$$

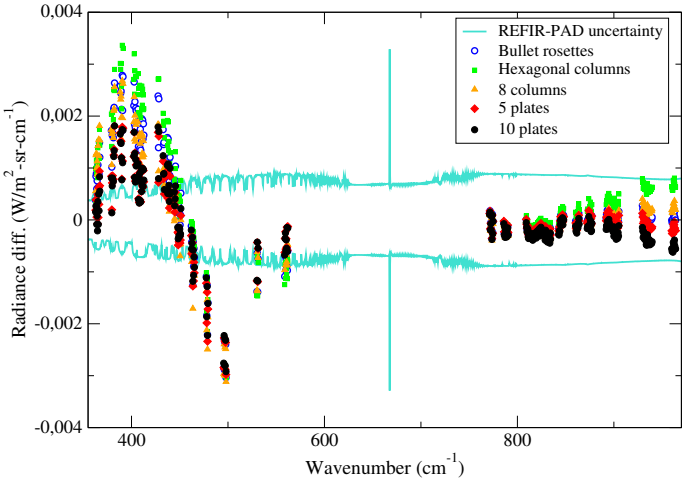

Figure 8. Comparison with respect of the averaged REFIR-PAD instrumental uncertainty (turquoise curves) of the mean differences between the measurements and the simulated spectra calculated in 28 selected microwindows reported in (Turner et al., 2003) for various ice crystal habits.

there is

We considered the retrievals good unless ~~we have~~ a reduced $\chi^2_{red} = \frac{\chi^2}{N-M} < 3$, with N number of spectral channels used and M number of retrieved parameters, as ~~done~~ in Di Natale et al. (2020).

The results of Fig. 8 show, as similarly done in Maestri et al. (2019), the retrievals performed with the different habits averaging the differences between the REFIR-PAD radiances and the simulated spectra in 28 microwindows reported in Turner et al. (2003), chosen between 360 and 970 cm^{-1} . We found that the aggregates of 10 plates show the best agreement with the measurements, with the lowest χ^2_{red}.

The left panel of Fig. 9 shows an example of the measurement of vertical reflectivity provided by the MRR on 27 January 2020 at 02:07 UTC, together with the lidar and REFIR-PAD measurements. The middle panel shows the lidar backscattering signal in arbitrary units (blue curve) and the depolarization (red curve). When the depolarization is higher than 15% the cloud is classified as ice cloud as described in Cossich et al. (2021). The right upper panel reports the REFIR-PAD measurement (black curve) in comparison with the simulated spectrum (red curve); the right lower panel shows the differences (green) in comparison with the instrumental uncertainty (black). The plot shows a very good agreement between the measurement and the simulation; the retrieval provides $D_{ei} = (121 \pm 4)$ μm , $L_m = (994 \pm 33)$ μm , $\text{OD}_i = (1.270 \pm 0.004)$, and χ^2_{red}=1.3.

4 Results and discussion

Fig. 10 shows the scatter-plots of L_m-N_o and OD_i-D_{ei} retrieved from REFIR-PAD (black circles). The L_m and N_o values allowed to obtained the PSD from Eq. (1), expressed in [$\text{m}^{-3}\text{mm}^{-1}$]. These values were used to derive the effective reflectivity Z_e at 24 GHz for the comparison with the MRR: the green circles in Fig. 10 denote the points detected by the MRR with

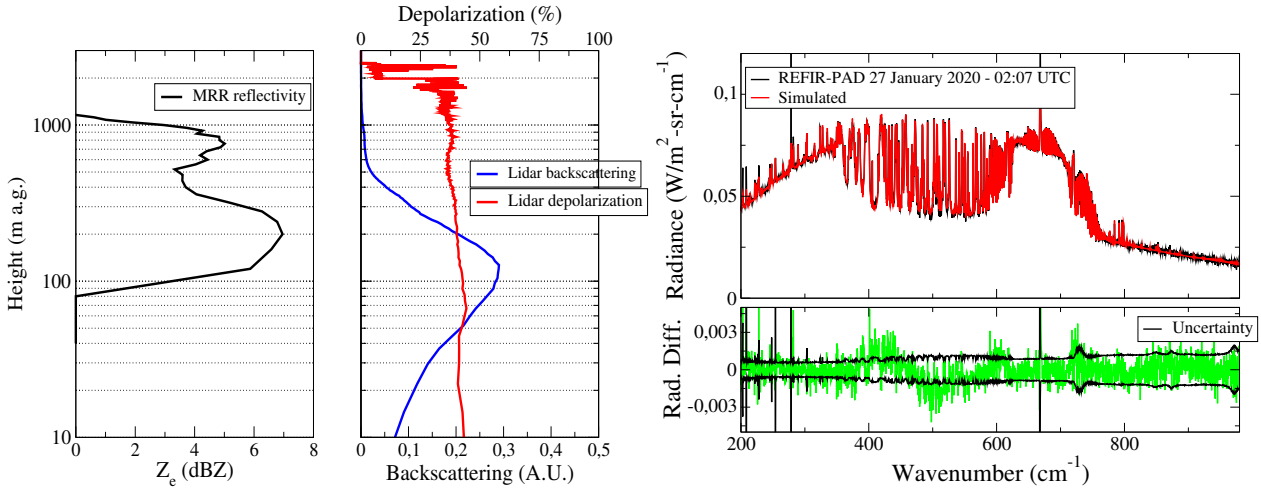

Figure 9. Left panel: reflectivity profiles provided by the MRR on the day 27 January 2020 at 02:07 UTC. Middle panel: backscattering (blue curve) and depolarization (red curve) lidar profiles. Right upper panel: comparison of a REFIR-PAD measurement (black curve) at 8:24 UTC on 10 December 2020 with the simulated spectra at the last iteration (red curve). Right lower panel: comparison of the differences between the measured and the simulated spectrum (green curve) with the instrumental noise (black curve).

reflectivity higher than -5 dBZ. We can see that the modal radius L_m of the maximum crystal length distribution varies mostly between 600–2000 μm ; the intercept N_o mostly stays in the range 10^4–10^{10} m^{-3}mm^{-8}.

The average crystal length can be calculated through the retrieved PSD as:

$$L_{\text{av}}^{\text{REFIR}} = \frac{\int_{L_{min}}^{L_{max}} L \cdot n(L) dL}{\int_{L_{min}}^{L_{max}} n(L) dL} \tag{18}$$

This value was used for the comparison with the crystal size estimated from the ICE-CAMERA measurements. The uncertainty is calculated by propagating the retrieval error in Eq. (18) and the one coming from the error in evaluating the CTH with the PT algorithm, which can be as large as 500 m in the worst cases. The CBH is considered not affected by error since it is always very close to the ground because we are treating precipitating events. If we indicate:

$$f_{l+1}(L_m) = \int_{L_{min}}^{L_{max}} L^{7+l} e^{-10\frac{L}{L_m}} dL \qquad \text{with } l = 0, 1 \tag{19}$$

the uncertainty $\Delta L_{\text{av}}^{\text{REFIR,ret}}$ due to the retrieval error turns out to be:

$$\Delta L_{\text{av}}^{\text{REFIR}} = \sqrt{\left|\frac{\partial L_{\text{av}}^{\text{REFIR,ret}}}{\partial f_1}\right|^2 \Delta f_1^2 + \left|\frac{\partial L_{\text{av}}^{\text{REFIR}}}{\partial f_2}\right|^2 \Delta f_2^2} \tag{20}$$

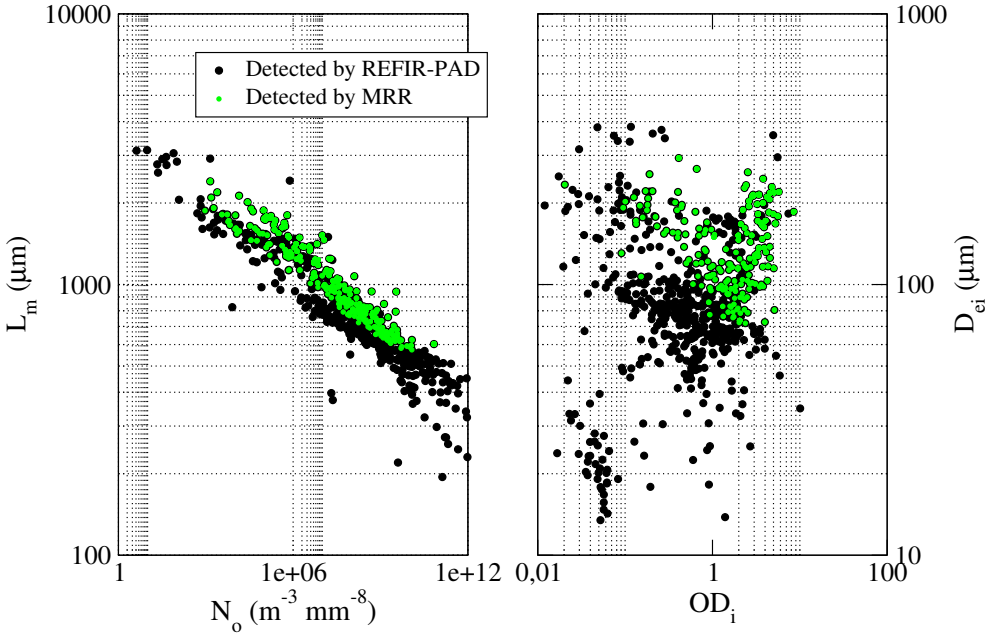

Figure 10. Left panel: scatter plot between the intercept N_o and the modal radius L_m of the particle size distributions retrieved from REFIR-PAD measurements. Right panel: scatter plot between the ice optical depth (OD_i) and the ice effective diameter (D_{ei}). The green circles denote the points detected by MRR. Just wondering how best to interpret these results since they are on a log-log scale…

with

$$\Delta f_{l+1} = \frac{10\Delta L_m}{L_m^2} \int_{L_{min}}^{L_{max}} L^{8+l} e^{-10\frac{L}{L_m}} dL \quad \text{with } l = 0, 1 \tag{21}$$

where ΔL_m denote the retrieval error of L_m.

The uncertainty $\Delta L_{\text{av}}^{\text{REFIR,CTH}}$ due to the CTH error is calculated by repeating the retrieval for each measurement increasing and decreasing this latter by 500 m; the maximum deviation from the original value of $L_{\text{av}}^{\text{REFIR}}$ is considered its associated uncertainty. The total uncertainty is finally calculated as follows:

$$\Delta L_{\text{av}}^{\text{REFIR}} = \sqrt{\left|\Delta L_{\text{av}}^{\text{REFIR,ret}}\right|^2 + \left|\Delta L_{\text{av}}^{\text{REFIR,CTH}}\right|^2} \tag{22}$$

4.1 Derivation of the equivalent radar reflectivity at 24 GHz

We can calculate the effective reflectivity at the MRR wavelength λ= 12.37 mm (24 GHz) by using the PSD retrieved from REFIR-PAD in the following formula (Eriksson et al., 2018; Tinel et al., 2005):

$$Z_e^{\text{REFIR}} = \frac{\lambda^4}{\pi^5 K_w^2} \int_{L_{min}}^{L_{max}} \sigma_{\lambda,h}(L, T_{cld}) n(L) dL \tag{23}$$

where K_w^2 = 0.92 is the dielectric constant of water and $\sigma_{\lambda,h}(L, T_{cld})$ is the backscattering cross section in [m^2] for the habit h at wavelength λ, T_{cld} in [K] is the cloud temperature, and L in [mm] as provided by the Eriksson et al. (2018) microwaves scattering database, which we name for simplicity EMD (for Eriksson Microwave Database). We set L_{max} equal to 10 mm as for the FIR properties and Z_e is expressed in [mm^{6}m^{-3}].

The backscattering cross sections are tabulated for 34 different habits, including liquid spheres and spherical graupel, and 17 of them are classified as single crystals, 3 habits represent heavily rimed particles, and the remaining habits are aggregates of different types, including snow and hail. Even though the particle sizes vary considerably among the habits, and the maximum length of 10 and 20 mm are typical values for the largest single crystal and aggregate particles, respectively, we limited the integral in Eq. (23) up to a cut-off value equal to 10 mm, corresponding to the maximum crystal length of the Yang et al. (2013) FIR database. The EMD is compiled with a broad coverage in frequency (1–886 GHz) for 3 values of temperature (190, 230 and 270 K), so that the final value can be obtained by interpolating. The temperature T_{cld} was calculated from the temperature profiles retrieved with SACR and the bounding heights CBH and CTH of the precipitating clouds.

The Z_e measured by the MRR was averaged along the vertical path ~~in order~~ to provide~~d~~ a parameter to compare with those retrieved from REFIR-PAD observations, which in turn represents an average over the cloud thickness:

$$Z_e^{\text{MRR}} = \frac{\int_{z_b}^{z_t} Z_e(z) dz}{\Delta z} \tag{24}$$

where z is the height.

Only MRR Z_e values above -5 dBZ were analyzed and included in the analysis, since below this value the results are not considered sufficiently reliable (Maahn and Kollias, 2012; Souverijns et al., 2017). In Table 1, we show results for all column-like, aggregates-like, and bullet rosette-like habits in EMD: the number of observations of REFIR-PAD measurements in coincidence with MRR which provide $Z_e > -5$ dBZ, the reduced χ^2_{red}, calculated considering the total error obtained for Z_e^{MRR} and $Z_e^{\text{REFIR-PAD}}$, and the correlation index r^2 between the MRR-observed and REFIR-PAD derived reflectivity.

We see that the habits ~~which~~ that maximize the number of points and r^2, and also minimize the χ^2_{red}, are the long columns and the thin columns for the column-like habits, the large block and large plate aggregates for aggregate-like habits, and 5/6 bullet rosette for bullet rosette-like habits. However, the habits ~~which~~ that maximize the number of points are the columns and the aggregates. Figure 11 shows the comparison of the MRR measured reflectivity with those obtained from REFIR-PAD by using the habits from EMD that provide the best match.

Finally, it should be noted that while the correlation coefficient turns out to be moderate (maximum ∼0.4), this is mostly due to the difficulty to retrieve with good accuracy the shape of the PSD from the FIR observations, and in particular the intercept N_o, for large particle sizes. However, the results indicate that in the particle size range between around 600 and 2000 μm , the retrieval algorithm is able to estimate the intercept with a correct order of magnitude as suggested by Fig. 11.

Table 1. Summary of the parameters obtained from the comparison of the REFIR-PAD and MRR reflectivity.

Habit name from Eriksson et al. (2018)	Number of observations	χ^2_{red}	r^2
	COLUMNS		
Long Columns	132	1.96	0.29
Thin Columns (ColTypeI)	68	1.22	0.26
Block Columns	253	10.31	0.39
ShortColumns	176	5.71	0.38
	AGGREGATES		
Large Block Aggregate	136	1.62	0.31
Large Column Aggregate	17	0.87	-0.17
Large Plate Aggregate	123	1.24	0.25
8 Columns Aggregate	111	3.89	0.31
Small Block Aggregate	46	1.99	0.10
Small Column Aggregate	0	-	-
Small Plate Aggregate	17	1.03	0.14
	BULLET ROSETTE		
5 Bullet Rosette	72	1.382	0.371
6 Bullet Rosette	89	1.586	0.165
Flat 3 Bullet Rosette	18	1.273	0.021
Flat 4 Bullet Rosette	25	0.985	0.293
Perpendicular 3 Bullet Rosette	25	0.994	0.281
Perpendicular 4 Bullet Rosette	25	1.020	0.295

4.2 Assessment of particle size and habit from ICE- and HALO-CAMERA

An average length of the ice crystals falling on the ICE-CAMERA screen can be defined by the area of the bounding box (A_{box}) containing the crystal itself as shown in Figs. 13 and 16 (red boxes). This parameter represents the diameter of the crystal with the projected area equal to the bounding box and it is calculated in μm (1 image pixel = 7 μm) by averaging ~~all~~ all of over the acquired crystals at the i-th scanning through the formula:

$$L_{\text{av}}^{\text{ICE-CAMERA}} = \frac{14}{N_c} \sum_{i=1}^{N_c} \sqrt{\frac{A_{\text{box},i}}{\pi}} \tag{25}$$

where N_c is the number of crystals acquired at the i-th scanning. The corresponding uncertainty is given by:

$$\Delta L_{\text{av}}^{\text{ICE-CAMERA}} = \frac{7 \Delta A_{\text{box}}}{N_c \sqrt{\pi}} \sqrt{\sum_{i=1}^{N_c} \frac{1}{A_{\text{box},i}}} \tag{26}$$

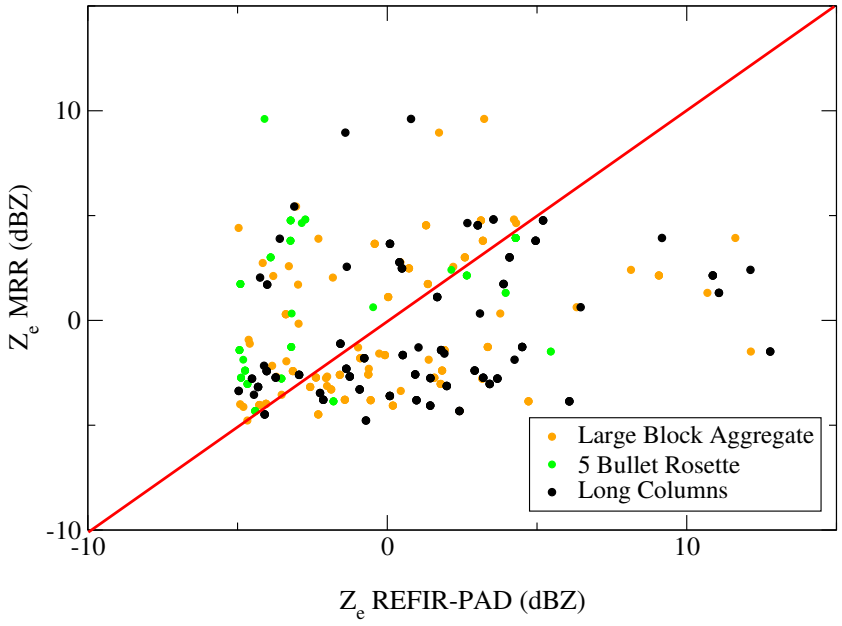

Figure 11. Scatter-plots of the Z_e measured by the MRR and those retrieved from REFIR-PAD obtained by using the habits from Eriksson et al. (2018) database which provide the best accordance: long columns, block columns aggregate and 5 bullet rosette.

where $\Delta A_{\text{box}} = \Delta A_{\text{box},i} \simeq 5$ pixel $\forall i$ is the uncertainty in pixel associated to each bounding box.

4.3 Selected days for case studies

We selected four days ~~on~~ in 2020, specifically 23/24 February and 21/24 April, when most of the measurements were simultaneously available, ~~in order~~ to be able to operate a specific comparison with the retrieved particle sizes.

4.3.1 Days 23 and 24 February 2020

The MRR reflectivity time-height cross-section for the selected days 23 and 24 February 2020 are shown on the left side of Fig. 12. The data are not continuous because of the filtering procedure due to the sensitivity of the MRR to the largest particles. The corresponding color map of the backscattering and depolarization lidar signals are also shown on the right of the same figure. The depolarization lidar shows that precipitation starts from the passage of ice clouds. The figure also shows the comparison of the average crystal length (L_{av}) retrieved from REFIR-PAD infrared spectra (red diamonds) with those obtained from the ICE-CAMERA (blue dots). Continuous MRR measurements and ICE-CAMERA data were available for the majority of both days as shown in Fig. 12.

Mixed-phase clouds did appear above the site on 23 February between 8–9 UTC and 12–13 UTC, where the presence of supercooled water is detected by the lidar depolarization at around 200 m above the ground.

The lower panels in Fig. 12 indicate that the values of the average crystal lengths retrieved from REFIR-PAD and those estimated from ICE-CAMERA are in very good agreement for most of the cases.

Would it be possible to draw a circle around the areas where there are supercooled liquid water clouds? If so, these clouds should be identified in the figure caption.

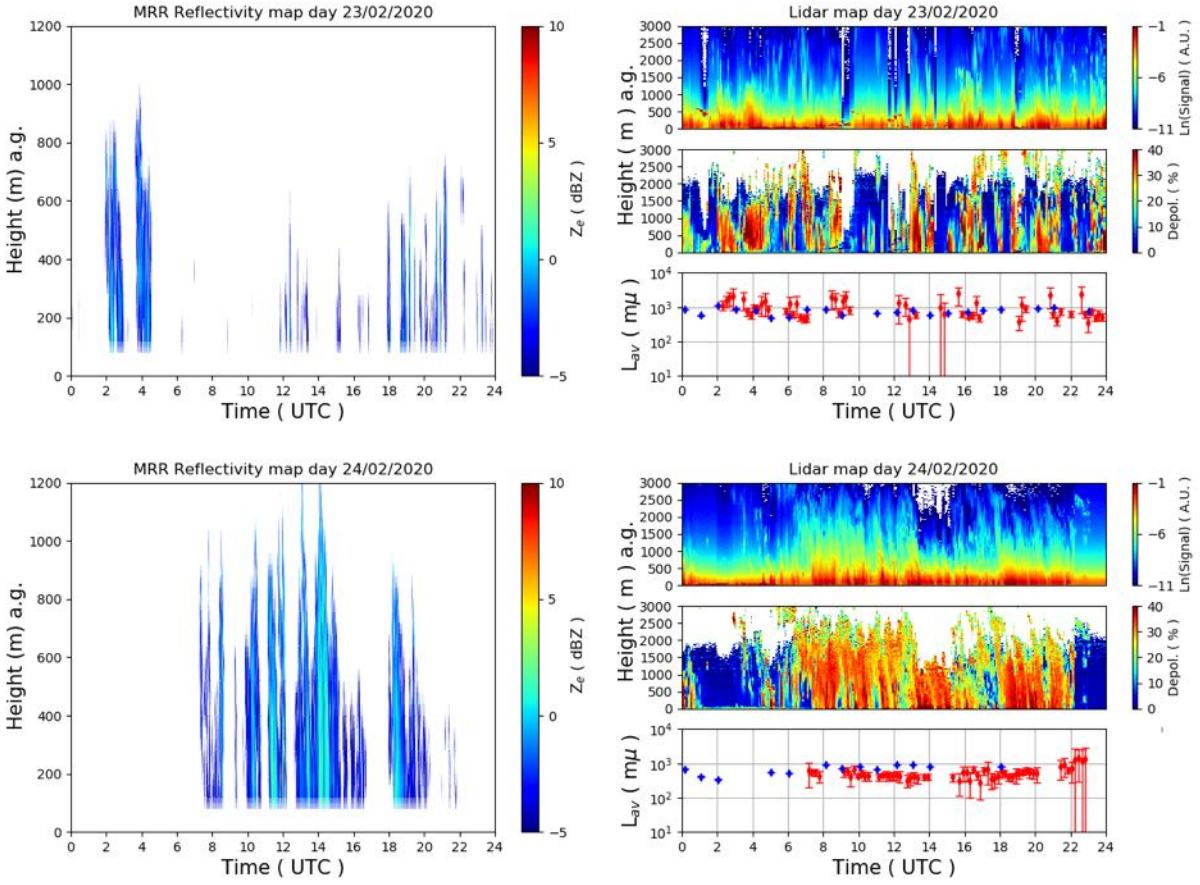

Figure 12. Left side: vertical profiles of reflectivity Z_e in dBZ obtained by the MRR as a function of the UTC time in hours of the days 23 and 24 February 2020. Right side: in the first and second upper panels are shown the backscattering and depolarization signals detected by the tropospheric lidar and in the lower panels is shown the comparison of the average crystals length of the ice crystals (L_{av}) retrieved from REFIR-PAD spectra (red diamonds) with those estimated from the ICE-CAMERA (blue dots).

Ice crystal pictures taken by the ICE-CAMERA in Fig. 13 indicates that the majority of the ice particles were column-like crystals with some complex aggregates. This is confirmed by the presence of distinct solar halos in the HALO-CAMERA images shown in Fig. 14.

Furthermore, the ICE-CAMERA crystal photographs and the halos recorded by the HALO-CAMERA sky images ~~confirm the best agreement found for columns-like and aggregate-like habits shown in Table 1~~.

provide an independent confirmation for the presence of columnar and aggregate habits, strengthening the analysis from the MRR and REFIR-PAD measurements.

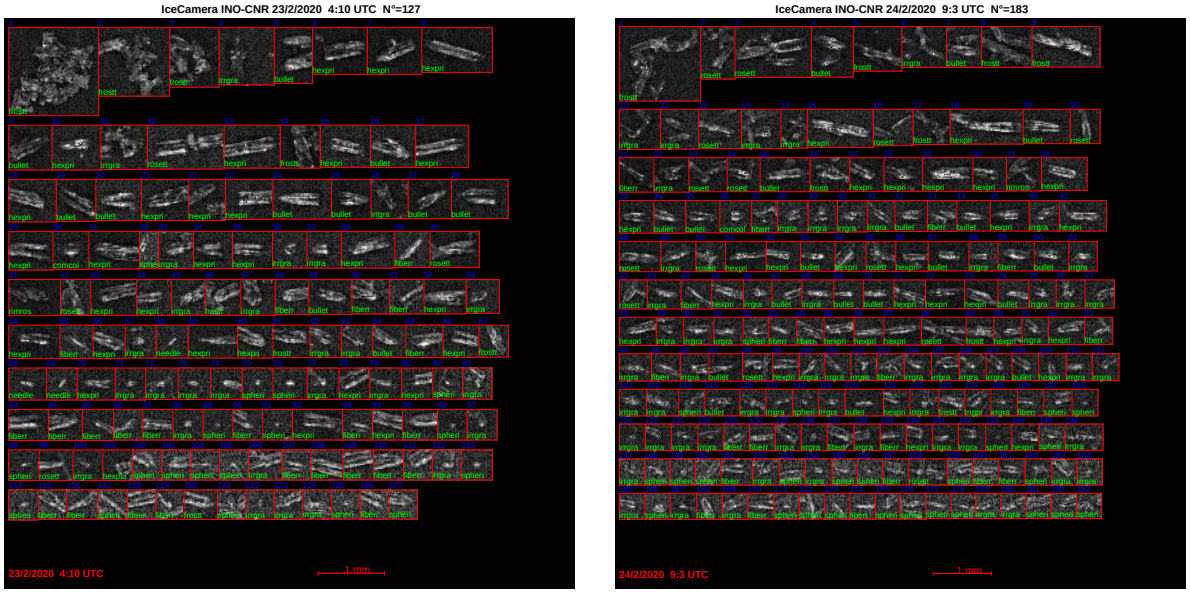

It would be helpful to the reader to include a brief interpretation of these subpanels - they are very small and it is difficult to see the detail. Perhaps show fewer of them so that the pictures are enlarged?

Figure 13. ICE-CAMERA photographs for the days 23 February (left side) and 24 February 2020 (right side).

Figure 14. HALO-CAMERA images for the days 23 February (left side) and 24 February 2020 (right side).

4.3.2 Days 21 and 23 April 2020

During 21 and 23 April 2020, some measurements from ICE-CAMERA were available for the comparison as shown in the lower panels of Fig. 15. Unfortunately, on the 23rd, only a single ice scan measurement was made by the ICE-CAMERA and it did not overlap in time with the radar data. However, the comparison for the 21 April shows ~~a~~ good agreement with the retrieved L_{av}. The MRR reflectivity shows high signal values, up to 8 dBz, between the 19:00 and 21:00 UTC for the 21 April and between the 06:00 and 11:00 UTC on 23 April. Fig. 16 shows photographs of of ice crystals from the ICE-CAMERA on both days, where ~~which~~ most of the ice is column-like crystals and rosettes with some complex aggregates. Also on 21 April, a mixed-phase cloud with supercooled water occurred between 17 and 20 UTC at about 1500 and 400 m above the ground.

Again, it would be helpful to the reader to draw a circle around the areas where there are supercooled liquid water clouds?
If so, these clouds should be identified in the figure caption.

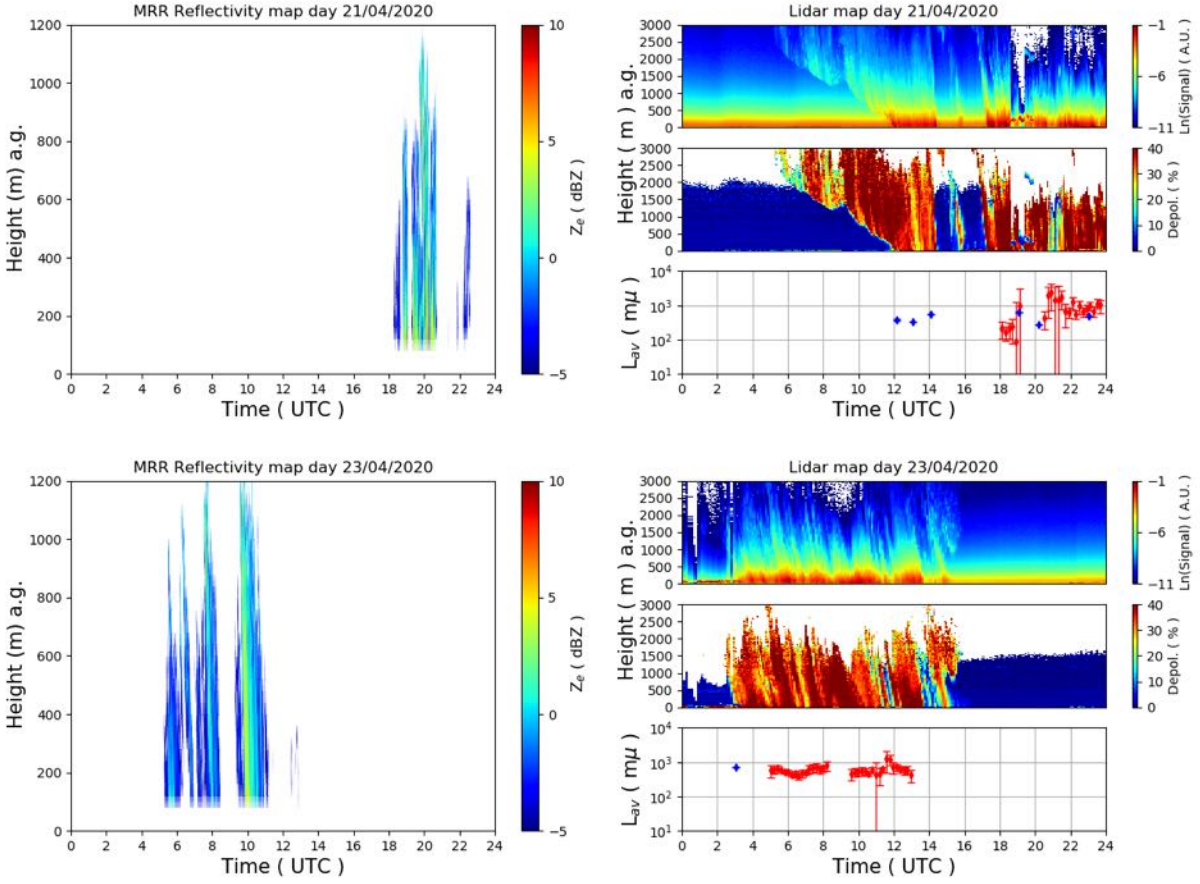

Figure 15. As for Fig. 12 but for the days 21 and 23 April 2020.

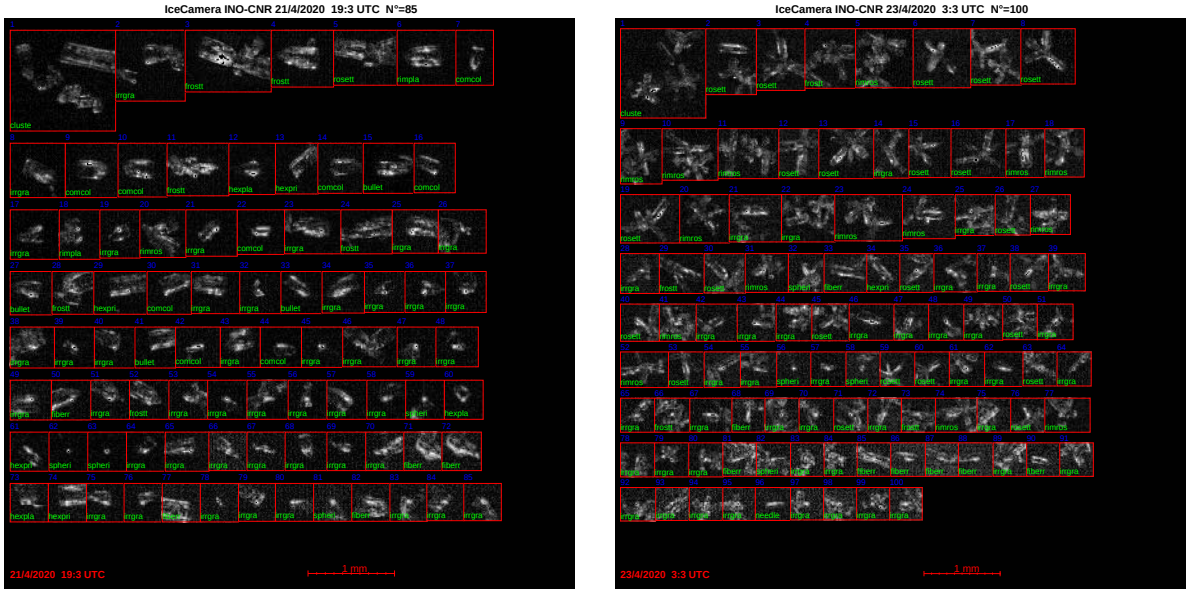

Perhaps show fewer sub panels and enlarge them so that the reader can see the details.

Figure 16. As for Fig. 13 but for the days 21 and 23 April 2020.

5 Conclusions and future perspectives

We presented a new approach to test the consistency of the retrieved ice cloud optical and microphysical properties during precipitating events at Dome-C, Antarctica, obtained from two separated portions of the atmospheric spectrum: in the microwave (24 GHz) the observations were provided by the Micro Rain Radar (MRR) while in the FIR, between 200-1000 cm^{-1} , the downwelling spectral radiance measurements were performed with the REFIR-PAD Fourier spectroradiometer.

The MRR was installed at Dome-C in 2018 and it has been operating in continuous and unattended mode since then. At the same location, the REFIR-PAD and the tropospheric backscattering lidar have been operating continuously since 2011 and 2008, respectively.

Cloud retrieval properties and the parameters of the particle size distributions were obtained from the synergistic use of the far infrared REFIR-PAD radiance spectra and the backscattering/depolarization lidar profiles.

The average crystal sizes of the precipitating particles were inferred from the photographs taken by the ICE-CAMERA, also installed at Dome-C. Furthermore, sky images provided by an HALO-CAMERA are used to detect the solar and lunar

halos generated by the ice crystals, allowed us to identify and discriminate some type of crystal habits responsible for the halos formation.

It is known that the sensitivity of the MRR is limited to the bigger falling particles (estimated around 1 mm), due to the large wavelength (12.37 mm) at which the MRR operates. For this reason, we restricted our study to a set of measurements, for now, over the first 2 years (2019–2020) of the radar measurements when the REFIR-PAD processed data were already consolidated. For large ice particles with sizes around 1 mm, the backscattering component of the infrared spectral radiance due to the ground emission is negligible. Furthermore, the dominant absorption component turns out to be independent of the crystal habit. We modelled the cloud with the aggregate-like crystal habit composed of 10 plates to simulate the radiative transfer and fit the radiance spectra with the Simultaneous Atmospheric and Cloud Retrieval (SACR) code, since for this type of habit the far infrared spectral radiance exhibits higher sensitivity. By analysing the depolarization of the backscattered lidar signal, we were able to assume that only ice was present, and to determine the top of the precipitating ice cloud through the Polar Threshold (PT) algorithm.

The retrieval procedure provided the cloud particle effective diameter and optical depth from which we could derive the intercept and the modal radius of the particle size distribution for each observation. These were used to calculate the effective reflectivity at 24 GHz through the scattering databases of Eriksson et al. (2018), which was then compared with MRR observations. The retrieved particle size distribution was also used to assess the mean length of the ice crystals and was compared with those inferred from the ICE-CAMERA images.

We found the best agreement between the reflectivity derived from the REFIR-PAD retrievals and the MRR observations when column-like (long columns) ice crystals habits and aggregates-like (large block aggregate) were used in the calculation of the reflectivity at 24 GHz. These habits show a maximum number of observations with $\chi^2_{\text{red}} \simeq 1$ and the correlation coefficient $r^2 \geq 0.3$. Even though the bullet rosette (5-bullet rosette) habits show a correlation coefficient of 0.37 with low chi square, the number of observations in accordance with the data is much lower with respect to the other. The differences arising in the column and aggregates were mostly due to the difficulty to retrieve the intercept parameter of the size distribution from FIR spectra in the presence of large particles. The high occurrence of hexagonal columns and aggregates was confirmed by the ICE-CAMERA photographs. In particular, the presence of hexagonal columns was confirmed by the 22°halos detected by the co-located HALO-CAMERA sky images as shown in previous studies at South Pole by Lawson et al. (2006). The agreement of both the retrieved parameters of the size distribution confirms that they correctly reproduced the data.

Furthermore, we found agreement in the ice crystal lengths between those derived from the REFIR-PAD retrievals and values derived from the ICE-CAMERA images. These results suggest, based upon the four days of data shown here, that the MRR has sensitivity to ice crystals as small as 600 μm of ice crystal length.

Because of the very low sensitivity of the MRR to the smallest particles, a drastic reduction of the data to be processed was necessary, partially limiting the impact of our study. However, as the instruments are all running operationally in an unatteded mode allows us the opportunity to collect a larger dataset, which can be used in future studies for confirming the results presented in this work and supporting further considerations with wider statistics.

Author contributions.

GDN conceptualized and designed the methodology and prepared the manuscript. DT conceptualized and designed the methodology. GDN, LP, GB and MDG installed and ran the instruments in Antarctica. AB, LB, LF and GDN prepared and performed MRR data analysis. GDN performed the REFIR-PAD, LiDAR and ICE-CAMERA data analysis. TM, WC and MM have contributed to design the methodology and the data analysis. GDN was responsible for the FIRCLOUDS project. All authors revised the manuscript.

Competing interests. The authors declare that they have no conflict of interest.

Acknowledgements. The authors gratefully acknowledge the Italian PNRA (Programma Nazionale di Ricerche in Antartide) and specifically the FIRCLOUDS (Far Infrared Radiative Closure Experiment For Antarctic Clouds) project, which provided funding support for the first author, and the DoCTOR (Dome-C Tropospheric Observer) program. Data and information on radio sounding measurements were obtained from the IPEV/PNRA Project "Routine Meteorological Observation at Station Concordia". We thank the mentioned institutions for supplying information about other measurements available at Concordia station.

References

Bailey, M. P. and Hallett, J.: A Comprehensive Habit Diagram for Atmospheric Ice Crystals: Confirmation from the Laboratory, AIRS II, and Other Field Studies, Journal of the Atmospheric Sciences, 66, 2888 – 2899, https://doi.org/10.1175/2009JAS2883.1, 2009.

Baran, A. J.: The impact of cirrus microphysical and macrophysical properties on upwelling far infrared spectra, Q. J. Roy. Meteor. Soc., 133, 1425–1437, 2007.

Baran, A. J.: A review of the light scattering properties of cirrus, J.Quant. Spectrosc. Radit. Transfer, 110, 1239–1260, 2009.

Bianchini, G., Palchetti, L., and Carli, B.: A wide-band nadir-sounding spectroradiometer for the characterization of the Earth's outgoing long-wave radiation, in Proc. SPIE 6361, Sensors, Systems, and Next-Generation Satellites X, 63610A, edited by R. Meynart, S. P. Neeck, and H. Shimoda, Stockholm, https://doi.org/10.1117/12.689260, 2006.

Bianchini, G., Castagnoli, F., Natale, G. D., and Palchetti, L.: A Fourier transform spectroradiometer for ground-based remote sensing of the atmospheric downwelling long-wave radiance, Atmos. Meas. Tech., 12, 619–635, https://doi.org/doi.org/10.5194/amt-12-619-2019, 2019.

Bracci, A., Baldini, L., Roberto, N., Adirosi, E., Montopoli, M., Scarchilli, C., Grigioni, P., Ciardini, V., Levizzani, V., and Porcù, F.: Quantitative Precipitation Estimation over Antarctica Using Different Ze-SR Relationships Based on Snowfall Classification Combining Ground Observations, Remote Sensing, 14, https://doi.org/10.3390/rs14010082, 2022.

Bromwich, D. H., Otieno, F. O., Hines, K. M., Manning, K. W., and Shilo, E.: Comprehensive evaluation of polar weather research and forecasting model performance in the Antarctic, Journal of Geophysical Research: Atmospheres, 118, 274–292, https://doi.org/https://doi.org/10.1029/2012JD018139, 2013.

Cossich, W., Maestri, T., Magurno, D., Martinazzo, M., Di Natale, G., Palchetti, L., Bianchini, G., and Del Guasta, M.: Ice and mixed-phase cloud statistics on the Antarctic Plateau, Atmospheric Chemistry and Physics, 21, 13 811–13 833, https://doi.org/10.5194/acp-21-13811-2021, 2021.

Costa, A., Meyer, J., Afchine, A., Luebke, A., Günther, G., Dorsey, J. R., Gallagher, M. W., Ehrlich, A., Wendisch, M., Baumgardner, D., Wex, H., and Krämer, M.: Classification of Arctic, midlatitude and tropical clouds in the mixed-phase temperature regime, Atmospheric Chemistry and Physics, 17, 12 219–12 238, https://doi.org/10.5194/acp-17-12219-2017, 2017.

Del Guasta, M.: ICE-CAMERA: a flatbed scanner to study inland Antarctic polar precipitation, Atmospheric Measurement Techniques Discussions, 2022, 1–35, https://doi.org/10.5194/amt-2022-62, 2022.

Di Natale, G., Palchetti, L., Bianchini, G., and Guasta, M. D.: Simultaneous retrieval of water vapour, temperature and cirrus clouds properties from measurements of far infrared spectral radiance over the Antarctic Plateau, Atmos. Meas. Tech., 10, 825–837, 2017.

Di Natale, G., Bianchini, G., Del Guasta, M., Ridolfi, M., Maestri, T., Cossich, W., Magurno, D., and Palchetti, L.: Characterization of the Far Infrared Properties and Radiative Forcing of Antarctic Ice and Water Clouds Exploiting the Spectrometer-LiDAR Synergy, Remote Sensing, 12, https://doi.org/10.3390/rs12213574, 2020.

Di Natale, G., Palchetti, L., Bianchini, G., and Ridolfi, M.: The two-stream δ-Eddington approximation to simulate the far infrared Earth spectrum for the simultaneous atmospheric and cloud retrieval, Journal of Quantitative Spectroscopy and Radiative Transfer, 246, 106 927, https://doi.org/https://doi.org/10.1016/j.jqsrt.2020.106927, 2020.

Di Natale, G., Barucci, M., Belotti, C., Bianchini, G., D'Amato, F., Del Bianco, S., Gai, M., Montori, A., Sussmann, R., Viciani, S., Vogelmann, H., and Palchetti, L.: Comparison of mid-latitude single- and mixed-phase cloud optical depth from co-located infrared spectrometer

and backscatter lidar measurements, Atmospheric Measurement Techniques, 14, 6749–6758, https://doi.org/10.5194/amt-14-6749-2021, 2021.

Eriksson, P., Ekelund, R., Mendrok, J., Brath, M., Lemke, O., and Buehler, S. A.: A general database of hydrometeor single scattering properties at microwave and sub-millimetre wavelengths, Earth System Science Data, 10, 1301–1326, https://doi.org/10.5194/essd-10-1301-2018, 2018.

Fan, S., Knopf, D. A., Heymsfield, A. J., and Donner, L. J.: Modeling of Aircraft Measurements of Ice Crystal Concentration in the Arctic and a Parameterization for Mixed-Phase Cloud, Journal of the Atmospheric Sciences, 74, 3799 – 3814, https://doi.org/10.1175/JAS-D-17-0037.1, 2017.

Garrett, T. J. and Zhao, C.: Ground-based remote sensing of thin clouds in the Arctic, Atmospheric Measurements and Techniques, 6, 1227–1243, 2013.

Harries, J., Carli, B., Rizzi, R., Serio, C., Mlynczak, M., Palchetti, L., Maestri, T., Brindley, H., and Masiello, G.: The Far Infrared Earth, Rev.Geophys., 46-RG4004, https://doi.org/10.1029/2007RG000233, 2008.

Intrieri, J. M., Fairall, C. W., Shupe, M. D., Persson, P. O. G., Andreas, E. L., Guest, P. S., and Moritz, R. E.: An annual cycle of Arctic surface cloud forcing at SHEBA, Journal of Geophysical Research: Oceans, 107, SHE 13–1–SHE 13–14, https://doi.org/10.1029/2000JC000439, 2002.

Keller, V. and Hallett, J.: Influence of air velocity on the habit of ice crystal growth from the vapor, Journal of Crystal Growth, 60, 91–106, https://doi.org/https://doi.org/10.1016/0022-0248(82)90176-2, 1982.

Kiehl, J. T. and Trenberth, K. E.: Earth's annual global mean energy budget, B. Am. Meteorol. Soc., 78, 197–207, 1997.

Korolev, A. and Isaac, G.: Phase transformation of mixed-phase clouds, Quarterly Journal of the Royal Meteorological Society, 129, 19–38, https://doi.org/https://doi.org/10.1256/qj.01.203, 2003.

Korolev, A., McFarquhar, G., Field, P. R., Franklin, C., Lawson, P., Wang, Z., Williams, E., Abel, S. J., Axisa, D., Borrmann, S., Crosier, J., Fugal, J., Krämer, M., Lohmann, U., Schlenczek, O., Schnaiter, M., and Wendisch, M.: Mixed-Phase Clouds: Progress and Challenges, Meteorological Monographs, 58, 5.1–5.50, https://doi.org/10.1175/AMSMONOGRAPHS-D-17-0001.1, 2017.

Lawson, R. P. and Gettelman, A.: Impact of Antarctic mixed-phase clouds on climate, Proc Natl Acad Sci, 111, 18 156–61, https://doi.org/10.1073/pnas.1418197111, 2014.

Lawson, R. P., Baker, B. A., Zmarzly, P., O'Connor, D., Mo, Q., Gayet, J.-F., and Shcherbakov, V.: Microphysical and Optical Properties of Atmospheric Ice Crystals at South Pole Station, Journal of Applied Meteorology and Climatology, 45, 1505–1524, https://doi.org/10.1175/JAM2421.1, 2006.

Lubin, D., Chen, B., Bromwitch, D. H., Somerville, R. C. J., Lee, W.-H., and Hines, K. M.: The Impact of Antarctic Cloud Radiative Properties on a GCM Climate Simulation, Journal of Climate, 11, 447–462, https://doi.org/10.1175/1520-0442(1998)011<0447:TIOACR>2.0.CO;2, 1998.

Maahn, M. and Kollias, P.: Improved Micro Rain Radar snow measurements using Doppler spectra post-processing, Atmospheric Measurement Techniques, 5, 2661–2673, https://doi.org/10.5194/amt-5-2661-2012, 2012.

Maesh, A., Walden, V. P., and Warren, S. G.: Ground-Based Infrared Remote Sensing of Cloud Properties over the Antarctic Plateau. Part I: Cloud-Base Heights, Journal of Applied Meteorology, 40, 1265–1277, 2001a.

Maesh, A., Walden, V. P., and Warren, S. G.: Ground-based remote sensing of cloud properties over the Antarctic Plateau: Part II: cloud optical depth and particle sizes, Journal of Applied Meteorology, 40, 1279–1294, 2001b.

Maestri, T., Rizzi, R., Tosi, E., Veglio, P., Palchetti, L., Bianchini, G., Girolamo, P. D., Masiello, G., Serio, C., and Summa, D.: Analysis of cirrus cloud spectral signatures in the far infrared, Journal of Geophysical Research, 141, 49–64, 2014.

Maestri, T., Arosio, C., Rizzi, R., Palchetti, L., Bianchini, G., and Del Guasta, M.: Antarctic Ice Cloud Identification and Properties Using Downwelling Spectral Radiance From 100 to 1400 cm-1, Journal of Geophysical Research: Atmospheres, 124, 4761–4781, https://doi.org/10.1029/2018JD029205, 2019.

Matrosov, S. Y., Orr, B. W., Kropfli, R. A., and Snider, J. B.: Retrieval of Vertical Profiles of Cirrus Cloud Microphysical Parameters from Doppler Radar and Infrared Radiometer Measurements, Journal of Applied Meteorology and Climatology, 33, 617 – 626, https://doi.org/10.1175/1520-0450(1994)033<0617:ROVPOC>2.0.CO;2, 1994.

Palchetti, L., Bianchini, G., Natale, G. D., and Guasta, M. D.: Far-Infrared radiative properties of water vapor and clouds in Antarctica, B. Am. Meteorol. Soc., 96, 1505–1518, https://doi.org/10.1175/BAMS-D-13-00286.1, 2015.

Palchetti, L., Natale, G. D., and Bianchini, G.: Remote sensing of cirrus microphysical properties using spectral measurements over the full range of their thermal emission, J. Geophys. Res., 121, 1–16, https://doi.org/10.1002/2016JD025162, 2016.

Platnick, S., Meyer, K. G., King, M. D., Wind, G., Amarasinghe, N., Marchant, B., Arnold, G. T., Zhang, Z., Hubanks, P. A., Holz, R. E., Yang, P., Ridgway, W. L., and Riedi, J.: The MODIS Cloud Optical and Microphysical Products: Collection 6 Updates and Examples From Terra and Aqua, IEEE Transactions on Geoscience and Remote Sensing, 55, 502–525, https://doi.org/10.1109/TGRS.2016.2610522, 2017.

Rathke, C., Notholt, J., Fischer, J., and Herber, A.: Properties of coastal Antarctic aerosol from combined FTIR spectrometer and sun photometer measurements, Geophysical research letters, 29, 46–1, 2002.

Ritter, C., Notholt, J., Fischer, J., and Rathke, C.: Direct thermal radiative forcing of tropospheric aerosol in the Arctic measured by ground based infrared spectrometry, Geophysical Research Letters, 32, https://doi.org/https://doi.org/10.1029/2005GL024331, 2005.

Rodgers, C. D.: Inverse methods for atmospheric sounding : theory and practice, World Scientific Publishing, 2000.

Rossow, W. B., Zhang, Y. C., and Columbia Univ., New York, N.: Calculation of surface and top of atmosphere radiative fluxes from physical quantities based on ISCCP data sets. 2: Validation and first results, Journal of Geophysical Research, 100, https://doi.org/10.1029/94JD02746, 1995.

Rowe, P. M., Cox, C. J., Neshyba, S., and Walden, V. P.: Toward autonomous surface-based infrared remote sensing of polar clouds: retrievals of cloud optical and microphysical properties, Atmospheric Measurement Techniques, 12, 5071–5086, https://doi.org/10.5194/amt-12-5071-2019, 2019.

Shupe, M. D., Daniel, J. S., de Boer, G., Eloranta, E. W., Kollias, P., Long, C. N., Luke, E. P., Turner, D. D., and Verlinde, J.: A Focus On Mixed-Phase Clouds: The Status of Ground-Based Observational Methods, Bulletin of the American Meteorological Society, 89, 1549 – 1562, https://doi.org/10.1175/2008BAMS2378.1, 2008.

Solomon, S.: Climate Change 2007-The Physical Science Basis: Working Group I Contribution to the Fourth Assessment Report of the IPCC, 4, 2007.

Souverijns, N., Gossart, A., Lhermitte, S., Gorodetskaya, I. V., Kneifel, S., Maahn, M., Bliven, F. L., and van Lipzig, N. P.: Estimating radar reflectivity-Snowfall rate relationships and their uncertainties over Antarctica by combining disdrometer and radar observations, Atmospheric Research, 196, 211–223, 2017.

Stone, R. S., Dutton, E., and DeLuisi, J.: Surface radiation and temperature variations associated with cloudiness at the South Pole, Antarct J Rev, 24, 230–232, 1990.

Tinel, C., Testud, J., Pelon, J., Hogan, R. J., Protat, A., Delanoë, J., and Bouniol, D.: The Retrieval of Ice-Cloud Properties from Cloud Radar and Lidar Synergy, Journal of Applied Meteorology, 44, 860 – 875, https://doi.org/10.1175/JAM2229.1, 2005.

Turner, D. D.: Arctic mixed-Phase cloud properties from AERI lidar observation: algorithm and results from SHEBA, Journal of Applied Meteorology, 44, 427–444, 2005.

Turner, D. D. and Mlawer, E. J.: The Radiative Heating in Underexplored Bands Campaigns, Bulletin of the American Meteorological Society, 91, 911 – 924, https://doi.org/10.1175/2010BAMS2904.1, 2010.

Turner, D. D., Ackerman, S. A., Baum, B. A., Revercomb, H. E., and Yang, P.: Cloud Phase Determination Using Ground-Based AERI Observations at SHEBA, Journal of Applied Meteorology, 42, 701–715, 2003.

Van Tricht, K., Gorodetskaya, I., Lhermitte, S., Turner, D., Schween, J., and Lipzig, N.: An improved algorithm for cloud base detection by ceilometer over the ice sheets, Atmospheric Measurement Techniques Discussions, 6, 9819–9855, https://doi.org/10.5194/amtd-6-9819-2013, 2013.

Yang, P., Mlynczak, M. G., Wei, H., Kratz, D. P., Baum, B. A., Hu, Y. X., Wiscombe, W. J., Heidinger, A., and Mishchenko, M. I.: Spectral signature of ice clouds in the far-infrared region: Single-scattering calculations and radiative sensitivity study, Journal of Gophysical Research, 108, 1–15, https://doi.org/10.1029/2002JD003291, 2003a.

Yang, P., Wei, H.-L., Baum, B. A., Huang, H.-L., Heymsfield, A. J., Hu, Y. X., Gao, B.-C., and Turner, D. D.: The spectral signature of mixed-phase clouds composed of non-spherical ice crystals and spherical liquid droplets in the terrestrial window region, J. Quant. Spectrosc. Radiat. Transfer, 79–80, 1171–1188, 2003b.

Yang, P., Huang, W. H., Baum, H.-L., Hu, B. A., Kattawar, Y. X., Mishchenko, G. W., I., M., and Fu, Q.: Scattering and absorption property database for nonspherical ice particles in the near-through far-infrared spectral region, Appl. Optics, 44, 5512–5523, 2005.

Yang, P., Bi, L., Baum, B. A., Liou, K.-N., Kattawar, G. W., Mishchenko, M. I., and Cole, B.: Spectrally Consistent Scattering, Absorption, and Polarization Properties of Atmospheric Ice Crystals at Wavelengths from 0.2 to 100 μm, Journal of atmospheric sciences, 70, 330–347, 2013.